J. Fluid Mech. (2019), *vol.* 871, *pp.* 401–426.
doi:10.1017/jfm.2019.313

Horizontal diffusive motion of columnar vortices in rotating Rayleigh–Bénard convection

D. Noto[1], Y. Tasaka[1,†], T. Yanagisawa[2,1] and Y. Murai[1]

[1]Laboratory for Flow Control, Faculty of Engineering, Hokkaido University, Sapporo, Japan

[2]Japan Agency for Marine-Earth Science and Technology (JAMSTEC), Yokosuka, Japan

(Received 18 November 2018; revised 6 March 2019; accepted 11 April 2019;
first published online 21 May 2019)

In laboratory experiments, horizontal translational motion of columnar vortices formed in rotating Rayleigh–Bénard convection was investigated. Two types of measurements, vertical velocity fields and horizontal temperature fields, were conducted with water as the test fluid. Using particle image velocimetry, the vertical velocity fields determined the parameter range at which the quasi-two-dimensional columnar vortices emerged. Locally, the duration characteristics of the columns, evaluated with their vertical coherence, indicate the minimum time scale of translational motion of the vortices in the horizontal plane. Vortex tracking of the horizontal temperature fields over long observation periods ($>10^3$ s) was conducted using encapsulated thermochromic liquid crystal visualization. Two cylindrical vessels with different radii showed the emergence of the centrifugal effect in $O(> 10^2$ s) despite the small Froude number ($Fr < 0.1$). Further, in the horizontal plane the columnar vortices behaved in a random-walk-like diffusive motion. The statistically calculated mean-squared displacements indicated anomalous diffusive motion of the columns; displacement increasing with time as t^γ with $\gamma \neq 1$. We discuss the causes of this anomaly in both the instantaneous and long-term statistical data gathered from experimental observations over different time scales. The enclosure effect from the repulsion of up-welling and down-welling vortices ensures that vortices diffuse only little, resulting in a sub-diffusive (decelerated) motion $\gamma < 1$ in $O(10^1$ s). With this weak centrifugal contribution, the translational motion of the columns slowly accelerates in the radial direction and thereby yields a super-diffusive (accelerated) motion $\gamma > 1$ in $O(10^2$ s).

Key words: Bénard convection, rotating flows, vortex dynamics

1. Introduction

Rayleigh–Bénard convection (RBC), the thermal convection driven between two horizontal plates at different temperatures, is a fundamental fluid mechanics system involving large-scale fluid motion. The addition of a background rotation to RBC, so-called rotating RBC, has attracted great worldwide interest applied to geophysical and astrophysical flows. Meteorological flows such as typhoons and tornadoes are examples of rotating RBC as the influence of the Earth's rotation here can then

† Email address for correspondence: tasaka@eng.hokudai.ac.jp

be understood intuitively (e.g. Meuel *et al.* 2012). In different scenarios, planetary magnetic fields are maintained by the convective motion of liquid metal influenced by the rotation in an outer core (Jones 2011; Grannan *et al.* 2016). For the physics of systems of large length scale and time scale, non-dimensional parameters such as Rayleigh and Taylor numbers would be large and cannot be directly assessed in direct numerical simulations (DNS) but require an asymptotically reduced equation valid in conditions of sufficiently fast background rotation (Sprague *et al.* 2006; Julien *et al.* 2012). The Rayleigh number, defined as the ratio of the thermal buoyancy to the viscous force, can be expressed in the form

$$Ra = \frac{g\beta\Delta T H^3}{\kappa\nu}, \tag{1.1}$$

where g, ΔT and H are the acceleration of gravity, the temperature difference between the top and bottom boundaries and the height of the fluid layer; β, κ and ν represent the thermal expansion coefficient, the thermal diffusivity and the kinematic viscosity. The effect contributed by rotation is frequently dictated by the Taylor number Ta, defined as the ratio of the Coriolis force to the viscous force and expressed by

$$Ta = \left(\frac{2\omega H^2}{\nu}\right)^2, \tag{1.2}$$

where ω is the angular velocity of the background rotation. Flow structures undergoing rotating RBC are commonly categorized with the convective Rossby number Ro, representing the contribution of the rotation relative to the thermal force:

$$Ro = \frac{1}{2\omega}\sqrt{\frac{g\beta\Delta T}{H}} = \sqrt{\frac{Ra}{Pr\ Ta}}. \tag{1.3}$$

To overcome the constraints imposed by computational limitations stemming from the widely distributed values of geophysical or astrophysical parameters, Sprague *et al.* (2006) proposed an asymptotic reduction for a rapidly rotating RBC. In this manner, smaller Ro conditions including actual geophysical or astrophysical states can be determined. For instance, Aurnou *et al.* (2015) predicted heat transport under conditions similar to interior Earth conditions by extrapolating the Nusselt and Rayleigh number (Nu–Ra) relation. The flow structures in rapidly rotating RBC ($Ro \ll 1$) have been investigated (Grooms *et al.* 2010; Stellmach *et al.* 2014; Cheng *et al.* 2015; Julien *et al.* 2016). Recent laboratory experiments have attempted to reach Ra and Ta regimes where asymptotic theory can be applied (Cheng *et al.* 2018). Here, the flow states in rapidly rotating RBC with Prandtl numbers $Pr = \nu/\kappa > 0.2$ may be categorized into four regimes. With decreasing Ro values, they are three-dimensional turbulence, vortical plumes, convective Taylor columns (CTCs) and cellular regimes identified by the variations in Nu (Liu & Ecke 2009; Weiss & Ahlers 2011; Julien *et al.* 2012; Stevens, Clercx & Lohse 2013). In vortical plumes and CTC regimes, the columnar vortex structures dominate the flow fields. Julien *et al.* (2012) established that steady columnar vortices do not emerge for $Pr \leqslant 3$. Prior to relatively recent works mentioned elsewhere, earlier reports had established the flow structures associated with transient regimes where the range of Ra is sufficiently large to induce finite-amplitude convection and also sufficiently small to yield prominent geostrophic flows. Under these conditions, up-welling and down-welling columnar

vortex behaviour is a result of the interplay between the surrounding columns (vortical plumes). Sakai (1997) reported on theoretical models describing the horizontal scale of columnar vortices at $Ro \sim 10^{0}$–10^{-1}. The motion of the columnar vortices was also recorded in the Sakai (1997) experimental reports. Further details of the vortex motion were reported in earlier work by Zhong, Ecke & Steinberg (1993). Here the mutual interactions (merging phenomena) of vortical structures in advection as time variations of the distance and angular orientation between two adjacent vortices were investigated, calculated from multiple vortex positions using flake visualization. Julien *et al.* (1996) presented a breakdown of the cellular roll state for $Ro = 0.75$ using DNS, and observed intense chaotic mutual interactions between vortices leading to merging and vanishing. Such mutual interactions were explained as the result of lateral mixing, which maintains an unstable horizontal mean temperature gradient in the fluid layer. Vorobieff & Ecke (1998, 2002) visualized spin-up states of rotating RBC and found advective motion of the vortical structures in the $0.2 < Ro < 1$ regime. Despite the many reports on such vortex motion, a detailed statistical analysis of the motion of columnar vortices has remained little understood.

In investigating vortex motion in a laboratory setting, the effect of centrifugal forces must be considered (Cheng *et al.* 2018). Conventionally, the Froude number is used to describe the effect of centrifugal forces. Defined as the ratio of the centrifugal force to the gravitational force,

$$Fr = \frac{L\omega^2}{2g}, \tag{1.4}$$

with L being the diameter of the cylindrical fluid layers, this factor cannot be disregarded in laboratory experiments because here the finite size of the fluid layers strongly influences the fluid motion. Horn & Aurnou (2018) analysed a wide range of DNS of Coriolis–centrifugal convection (C^3), and discussed centrifugal forces by defining a centrifugal Rossby number, $Ro_c = Ro\sqrt{2Fr/\Gamma}$, where Γ denotes the aspect ratio of the fluid layer given as $\Gamma = L/H$. In such arrangements, centrifugally dominated convection occurs for $Fr > \Gamma/2$. To be able to disregard centrifugal effects, the aspect ratio of the fluid vessel must be small in rapidly rotating RBC (Cheng *et al.* 2018). For empirical criteria, a condition with $Fr < 0.1$ is thought to allow disregarding the contribution of centrifugal force in rotating RBC; however, this has not been finally verified. One reason is the long time scales of the effects of centrifugal buoyancy $O(10^2$–10^3 s) in laboratory settings (Horn & Aurnou 2018). Noto *et al.* (2018) established a vortex detection method employing visualization of instantaneous temperature fields enabling the prolonged tracking of columnar vortices. In conventional vortex identification, values for the velocity fields must be established because the vortex structures may be determined by the vorticity fields or other quantities such as the Q criteria (Kunnen, Clercx & Geurts 2010; Stevens, Clercx & Lohse 2012; Kunnen, Corre & Clercx 2014). Particle image velocimetry (PIV) is a commonly applied method to measure two-dimensional (2-D) velocity fields. This method measures the instantaneous velocity vector field by identifying local similarities between two sequential images captured within a short time interval. Here the time interval required depends on the flow velocity, and typically rates of 10–100 frames per second (f.p.s.) are used for thermal convection measurements. Without considering appropriate time intervals to track vortices, data storage and/or computational load would be potential difficulties. In addition, the spatial resolution of the velocity (vorticity or Q-value) fields become less detailed than the original digital images. Thus, a PIV approach does not necessarily suit measurements of

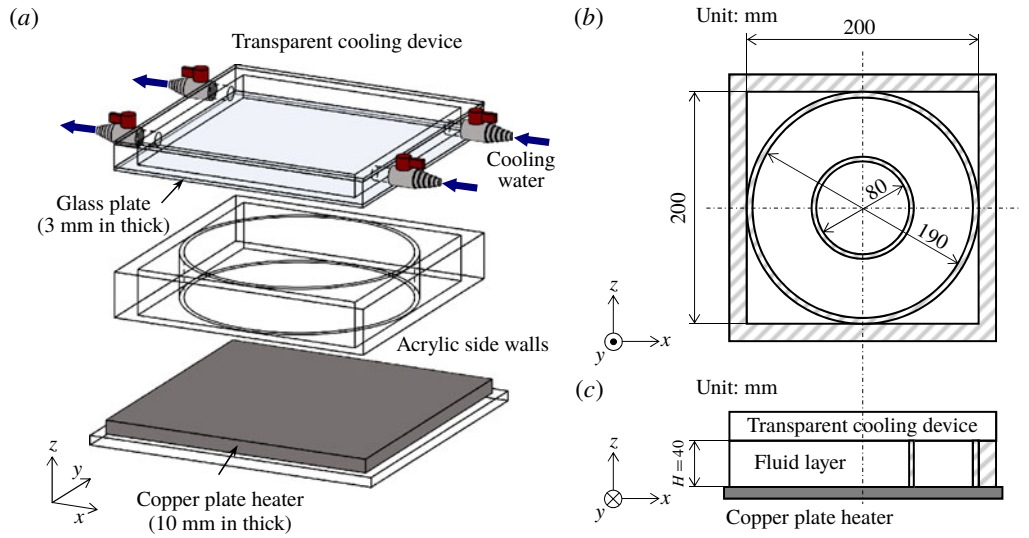

FIGURE 1. (Colour online) Schematic diagram of the fluid vessel. (*a*) Overview of the vessel with the acrylic walls, cooling device and copper plate heater. The cylinder inside the square-walled vessel is of diameter $L = 190$ mm. (*b*) Horizontal cross-section of the vessel, where two different cylinders ($L = 80$ or 190 mm) are alternatively placed. (*c*) Vertical cross-section of the vessel.

vortex motion conducted over extended time periods: from such considerations the method proposed by Noto *et al.* (2018) becomes advantageous.

The objective of this study is to establish the translational motion of the quasi-2-D columnar vortices formed in rotating RBC with and without centrifugal force effects based on the measurement technique established in Noto *et al.* (2018). The flow regimes at $Ro \sim 10^{0}$–10^{-1} are chosen to display the active motion of the columns, as reported previously (Zhong *et al.* 1993; Julien *et al.* 1996; Sakai 1997). In these regimes, it has not been established whether the conventional criteria identifying the four different flow regimes apply to laboratory experiments. To ensure the generation of columnar vortices in the parameter ranges investigated, the flow structures in the vertical cross-sections were initially investigated by measuring the velocity fields. Under conditions where columnar vortical structures develop, the horizontal motion of these structures, labelled by the method proposed in Noto *et al.* (2018), was tracked for longer than 10^{3} s. Finally, a detailed discussion of the horizontal translational motion of the columnar vortices is presented based on the results of the statistical analyses here.

2. Experimental set-up and measurement method

2.1. *Experimental set-up*

The fluid vessel used in the present study is shown in figure 1. The side walls enclose an acrylic square vessel 200 mm wide and 40 mm high. A cylindrical fluid layer of the same height, $H = 40$ mm, was formed by placing one of two acrylic cylinders (diameters $L = 80$ and 190 mm) in the square vessel allowing easy change in the horizontal geometries. Degassed distilled water ($Pr \sim 7$ at 20 °C) was used as the test fluid. A 10 mm thick copper plate heater was set under the bottom of the

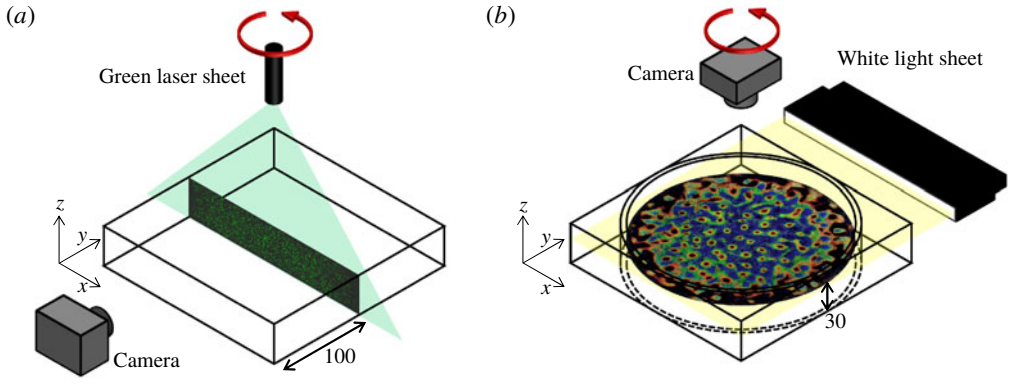

FIGURE 2. (Colour online) Optical arrangements for (*a*) the vertical velocity field measurements by PIV and (*b*) the horizontal temperature field measurements by TLC particles. Images embedded in each panel are examples obtained by these two different visualization methods. For the experiments, the fluid vessel and optical equipment were placed on a platform and rotated as suggested by the top arrows (red online).

vessel. Isothermal heating was maintained by controlling the electric current supplied to the heater. The top surface of the vessel was cooled by circulating water from a thermostatic bath via a 3 mm thick glass plate. The corresponding Biot number in the present study is around 0.6 (Noto *et al.* 2018), and preliminary experiments verified the homogeneity of the top cooling condition with this glass plate thickness. The effective temperature difference across the fluid layer was $\Delta T = 11.1\,^{\circ}\mathrm{C}$ measured by thermistors located at the bottom of the copper plate and right beneath the top glass plate. The fluid vessel and all the optical equipment including a camera were mounted on a rotating platform (1 m in diameter with two stages, not shown in figure 1) and rotated together with the vessel and plates. A detailed description of the present experimental apparatus for this rotating RBC is given elsewhere (Noto *et al.* 2018). The angular velocity ω realized by this set-up is 0.0 to 5.0 rad s^{-1}, corresponding to $Ta = 0.0\text{–}2.8 \times 10^8$. Using different configurations of the optical equipment as suggested in figure 2, two different series of experiments were conducted: velocity field measurements of a vertical cross-section (figure 2*a*) and temperature field measurements of a horizontal cross-section (figure 2*b*). Details of the experiments are described separately in the following sections.

2.2. *Velocity field measurements on a vertical cross-section*

To perform the PIV measurements of the velocity field on a vertical cross-section, a 2 W green laser sheet (<5 mm thick) is illuminated from above the cross-section at the middle position ($y = 2.5H$, 100 mm) of the fluid layer (figure 2*a*). No cylinders were placed in the acrylic vessel during the PIV measurements. A small amount of porous resin particles (mean diameter $d_p = 90\ \mu\mathrm{m}$, mean density $\rho_p = 1.02 \times 10^3\ \mathrm{kg\ m}^{-3}$, HP20SS, Mitsubishi Chemical Co.) were dispersed into the test water and used as flow tracers. The Stokes number $St = \rho_p d^2 U/(18\rho\nu H)$ is $O(10^{-4}) \ll 1$, with ρ the density of the working fluid and U the representative flow velocity (to be detailed below); this will ensure that the tracer particles follow the fluid motions closely. From one side of the vessel, particle images in the x–z plane were recorded using a digital camera (EXF1, Casio) at 5 f.p.s. and a resolution of

0.1 mm pixel^{-1} (2000 pixels $\times$ 400 pixels for 200 mm $\times$ 40 mm). The images were processed using a standard cross-correlation method to derive instantaneous velocity vector fields from two sequential images.

2.3. *Temperature field measurements on a horizontal cross-section*

For the temperature field visualization, a white light sheet generated by a halogen lamp illuminated a horizontal cross-section at a set height, $z = 0.75H$ (30 mm), of the fluid layer (figure 2*b*). A camera, the same as the one used for the PIV experiments, was set at the axis of rotation and recorded colour images of the x–y plane from above the fluid layer. Encapsulated thermochromic liquid crystal (TLC) particles (mean diameter $d_p = 15$ µm, mean density $\rho_p = 1.02 \times 10^3$ kg m^{-3}, approximate dynamic range 20–25 °C, Japan Capsular Products Inc.) were suspended in degassed water for the temperature field visualization. Estimated St, $O(10^{-6})$, ensures sufficiently high traceability of the TLC particles. An example of a temperature field visualized by TLC at no-rotation conditions ($Ra = 1.0 \times 10^7$ and $Ta = 0$) obtained in the larger vessel is shown in figure 3. The TLC shows coloration corresponding to the temperature by the scattered incident white light. Typically, red is at the lower end of the colouring temperature range, and the TLC changes scattering colour, from green to light blue to dark blue, as the temperature increases. As shown in figure 3, it is possible to observe red-coloured, cold down-welling flows, and blue-coloured, warm up-welling flows showing the large-scale structures in this condition. The working fluid filled the entire fluid layer including the corner regions outside the cylinders. As a result, the temperature of the ambient fluid is controlled within the set temperature differences playing the role of a water jacket, as well as reducing unwanted reflection of the incident light and provides better quality colour images. The colour images were acquired at three-second intervals ($\Delta t = 3$ s, 1/3 f.p.s.) with an f-number of 2.7, and a resolution of 0.1 mm pixel^{-1} for $\Gamma = 2.00$ and 0.1357 mm pixel^{-1} for $\Gamma = 4.75$. The TLC is useful for observing the fluid temperature non-invasively. Its calibration from the colour information to temperature is influenced by a number of uncertainties (Wiberg & Lior 2004; Abdullah *et al.* 2010; Rao & Zang 2010). For instance, sensitivity to the incident light yields colorations with a strong dependence on image positions, and the observation direction (the angle measured from the lens) induces similar colour inhomogeneities. To overcome these TLC measurement difficulties, the present study employed localized hue calibration to obtain the temperature fields and applied a robust vortex detection method (Noto *et al.* 2018). In this, the temperature at each pixel was calibrated from locally obtained hue–temperature calibration curves. By combining the vortex detection method with this calibration, it is possible to identify columnar vortices from horizontal temperature fields as undulations at $Pr \sim O(1)$.

3. Development of quasi-2-D columnar vortices

3.1. *Vertical coherence of vortical structures*

Columnar vortical structures, the main focus of the present study, are observed in the transition from a three-dimensional thermal turbulence regime to a CTC regime via a vortical plume regime (Grooms *et al.* 2010). The emergence of the columnar vortices requires (quasi-)geostrophic conditions that are conventionally assumed at $Ro \ll 1$. But the parameter boundaries between the regimes must be evaluated in detail in the experiments, and are considerably influenced by side boundaries and centrifugal forces. Consequently, five different conditions, as detailed in table 1,

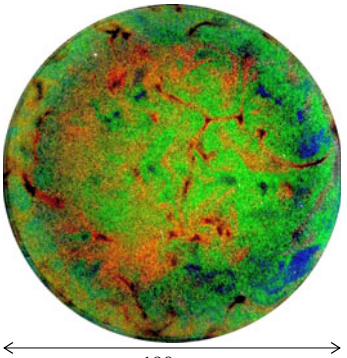

FIGURE 3. (Colour online) An example of a horizontal temperature field visualized using the encapsulated TLC at $z = 0.75H$ for $Ra = 1.0 \times 10^7$ and $Ta = 0$ recorded in the $\Gamma = 4.75$ vessel.

Pr	Ra	Ta	Ro	Fr	N_{vortex}	
					Up-welling	Down-welling
		1.0×10^6	1.20	1.0×10^{-3}	16.0	52.6
		6.0×10^6	0.49	6.0×10^{-3}	—	—
~ 7 (at 20 °C)	1.0×10^7	1.0×10^7	0.38	1.0×10^{-2}	74.7	114.2
		6.0×10^7	0.15	6.0×10^{-2}	—	—
		1.0×10^8	0.12	1.0×10^{-1}	198.8	214.2

TABLE 1. Parameter settings for the vertical velocity measurements, and measurements of the number of up-welling and down-welling vortices, from Noto *et al.* (2018).

were investigated to evaluate details of the emergence of columnar vortices by PIV measurements. Due to the limitations of the turntable, Ro distributes from 1.20 to 0.12 for the set Rayleigh number, $Ra = 1.0 \times 10^7$, in the test conditions here. In the following, N_{vortex} is the number of columnar vortices determined in the temperature field image at the horizontal cross-sections of $z = 0.75H$ inside a cylinder with $\Gamma = 4.75$ (Noto *et al.* 2018). The number of heated vortices present under very similar conditions, $Ro = 0.1$–10, in the DNS conducted by Pieri *et al.* (2016), is similar to that obtained here (see table 1). Typically, N_{vortex} increases with decreasing Ro, and N_{vortex} strongly depends on the vertical height position. To quantify the vertically distributed characteristics, Rajaei, Kunnen & Clercx (2017) reported an increase in the vertical coherence with decrease in Ro by PIV experiments. This suggests that the development of columnar vortices may be observed in decreasing Ro conditions in the images of the vertical velocity fields.

Examples of the velocity vector distributions measured in the x–z plane at $y = 2.5H$ for each Ta setting are shown in figure 4. Here, the magnitude of the measured velocity $\sqrt{u^2 + w^2}$ is rendered in grey scale. Flow structures at low Ta settings, as in figure 4(*a*–*c*) are not well organized along the direction of the rotational axis, and only some column-like structures are visible. At high Ta settings (figure 4*d*,*e*), flow structures are recognizable as separate columns. A representative flow velocity is given by Prandtl's free-fall theory, $U_f = \sqrt{g\beta\Delta TH}$, and here estimated at roughly

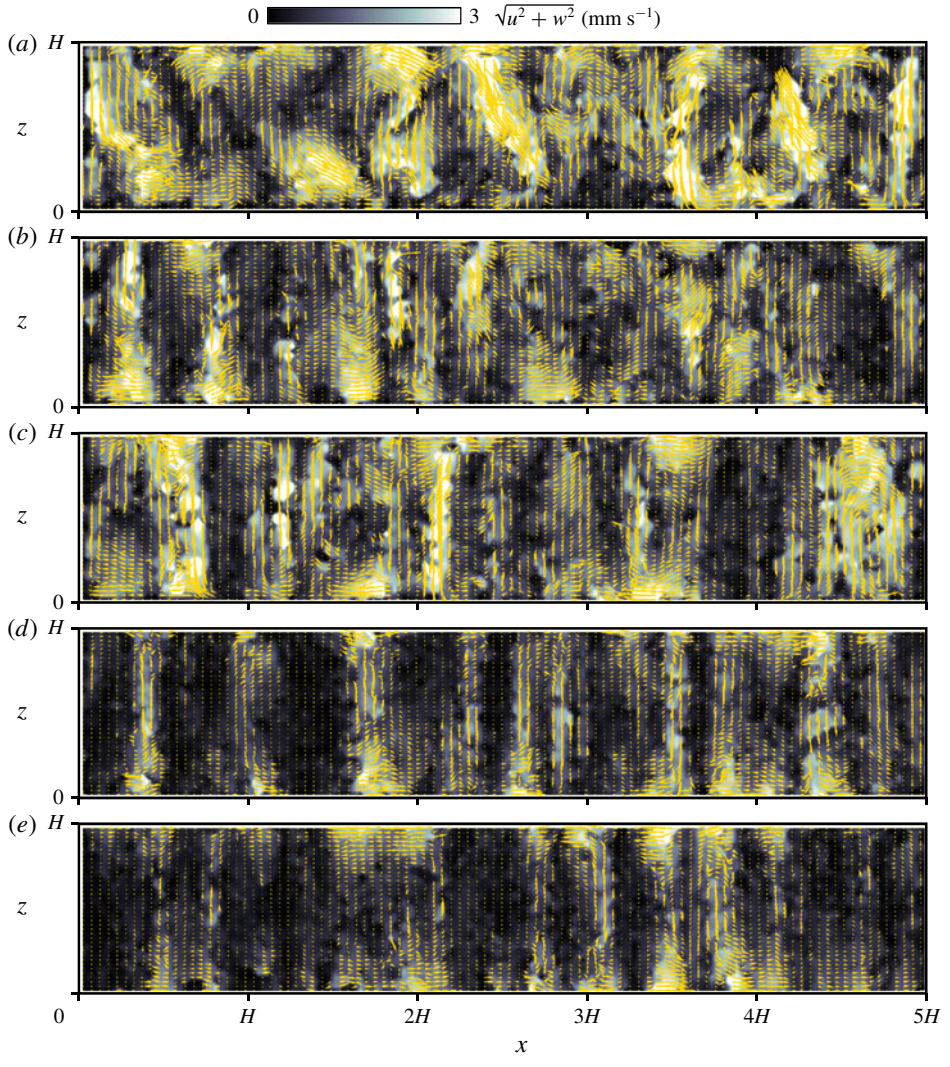

FIGURE 4. (Colour online) Snapshots of the velocity vector distributions of vertical cross-sections measured in PIV at $y = 2.5H$: (*a*) $Ta = 1.0 \times 10^6$ ($Ro = 1.20$), (*b*) $Ta = 6.0 \times 10^6$ (0.49), (*c*) $Ta = 1.0 \times 10^7$ (0.38), (*d*) $Ta = 6.0 \times 10^7$ (0.15) and (*e*) $Ta = 1.0 \times 10^8$ (0.12). Only every second vector (the slanted short line (yellow online)) is plotted for clearer visibility.

$U_f \sim 30$ mm s^{-1}. The magnitude of the velocity in rotating RBC is small, at almost only one-tenth of U_f because the background rotation is suppressed even when Ta is the smallest. This is also indicated from the fact that the magnitude of the velocity for higher Ta values is lower than that for lower Ta. A typical geostrophic velocity proposed by Sakai (1997), U_0, reflecting a geostrophic balance in the fluid interior, may be obtained from

$$U_0 = \frac{\kappa}{2l}\left(\frac{\Delta T_c}{\Delta T}\right) RaTa^{-1/2}, \tag{3.1}$$

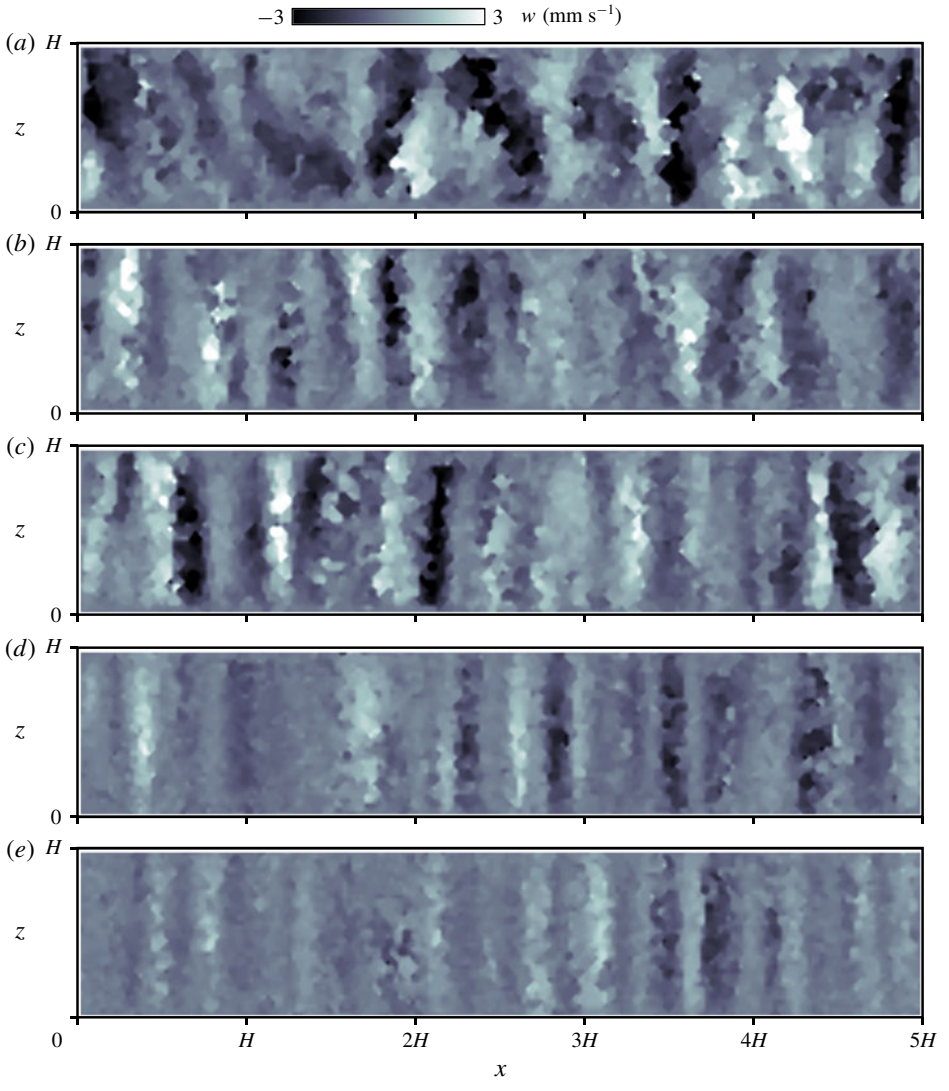

FIGURE 5. (Colour online) Vertical velocity distributions $w(x, z)$ in vertical cross-sections at the same moment as that of figure 4 measured by PIV at $y = 2.5H$: (*a*) $Ta = 1.0 \times 10^6$ ($Ro = 1.20$), (*b*) $Ta = 6.0 \times 10^6$ (0.49), (*c*) $Ta = 1.0 \times 10^7$ (0.38), (*d*) $Ta = 6.0 \times 10^7$ (0.15) and (*e*) $Ta = 1.0 \times 10^8$ (0.12).

where ΔT_c is the temperature difference between up-welling and down-welling vortices when the vertical temperature of the columns is constant, and the columns are separated by a distance l. Under the present conditions, U_0 is of order $O(1\ \mathrm{mm\ s^{-1}})$, which would agree well with the present results.

To highlight the vertical coherence of the flow structures, the corresponding distributions of the vertical velocity w for the images shown in figure 4 were also calculated and are shown in figure 5. While somewhat disorganized, structures are visible in figure 5(*a*). These are vertical coherent structures from bottom to top (bright), and from top to bottom (dark), aligned alternately in horizontal directions in

the other cases satisfying $Ro < 1$. These indicate up-welling and down-welling flows that arise from Ekman pumping. The structures appear increasingly regularized in the vertical direction with increasing Ta; the horizontal distance (left–right in the figure) between the structures also becomes shorter. In a previous report (Noto *et al.* 2018), the distance between neighbouring structures at each setting was found to agree well with the theory established by Sakai (1997). Fluctuations of the velocity in the vertical direction diminish with Ta with the structure appearing as a quasi-2-D regular column in figure 5(*d*,*e*), specifically, at $Ro = 0.15$ and 0.12. Further quantitative criteria to distinguish prominent columnar vortices are discussed in the next section.

3.2. *Local duration characteristics of columnar vortices*

In the previous section, spatial, instantaneous quasi-2-D columnar structures were analysed. To investigate the translational motion of columnar vortices, the duration of vertical coherence also needs to be investigated in regard to the time variation in the appearance. This is required to verify that the vortices detected on the horizontal plane in sequential images exhibit translational motion and not a continuous skewed deformation. This also has importance in determining a suitable time resolution for vortex tracking. One advantage of TLC visualization is that detection of the vortices may be achieved from a single instantaneous image with a wider flexible range of time resolutions than in PIV requiring two consecutive images taken within a short time interval (Noto *et al.* 2018).

Considering the results obtained with PIV, in particular those in figure 5(*d*,*e*), the sign of the vertical velocity w along a single columnar vortex is the same from top to the bottom and in the image. This is because all the columnar vortices can be classified as up-welling ($w > 0$) or down-welling ($w < 0$) vortices. As Rajaei *et al.* (2017) showed, vertical coherence of columnar vortices can be obtained by making auto-correlations of vorticity along the rotational axis, when all of the velocity information (three-dimension and three-component) is available. In the present study, the available information is the velocity field only in the x–z plane, and it is necessary to show vertical coherence of the columnar vortices in this condition. Hence, the averaged vertical velocity $\overline{w(x,t)} = (1/H)\int_0^H w(x,z,t)\,\mathrm{d}z$ is a useful indicator to identify column formation. To establish the time variation of the vertical coherence, the evolution of $\overline{w(x,t)}$ with elapsed time is plotted (figure 6). In figure 6 the values have been normalized using the maximum of the absolute value. The two-headed arrows in each panel are equivalent to the theoretically predicted diameters of the vortices, L_{vortex}, derived by Sakai (1997) and as will be defined below. In figure 6(*a*,*b*), the bright and dark stripes do not maintain the same width throughout the observation period. A zero value of $\overline{w(x,t)}$ indicates the absence of columns. With a larger Ta setting, figure 6(*c*–*e*) shows a straight striped pattern. The columns appear at very similar positions, at least within the observation period for the larger Ta settings here. In addition, there are variations in the width of the stripes. Assuming that the widths of the columnar vortices are constant in the horizontal direction, these variations arise from plane displacements, specifically, column displacements in the y direction; skewed stripes indicate displacements in the x direction.

Assuming that the horizontal motion of the vortices is isotropic, the advection speed of the columnar vortices may be estimated simply from the slopes of the stripes:

$$v_{adv} = \sqrt{\left(\frac{\mathrm{d}x}{\mathrm{d}t}\right)^2 + \left(\frac{\mathrm{d}y}{\mathrm{d}t}\right)^2} \sim \sqrt{2\left(\frac{\mathrm{d}x}{\mathrm{d}t}\right)^2}, \tag{3.2}$$

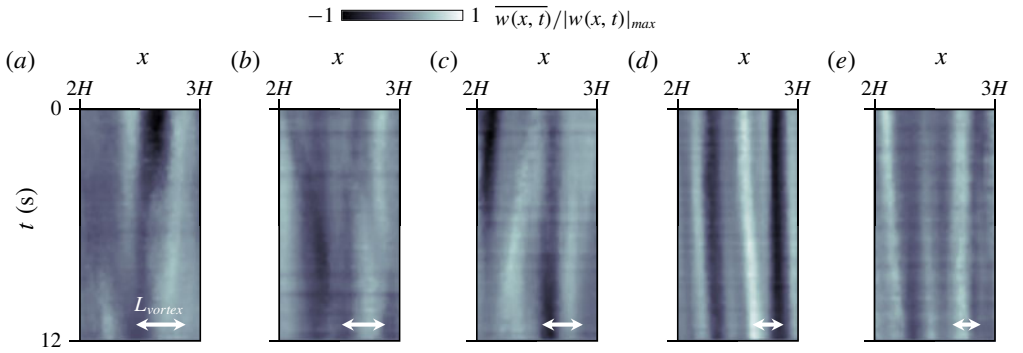

FIGURE 6. (Colour online) Time series of averaged vertical velocities at horizontal positions $2H < x < 3H$: (*a*) $Ta = 1.0 \times 10^6$ ($Ro = 1.20$), (*b*) $Ta = 6.0 \times 10^6$ (0.49), (*c*) $Ta = 1.0 \times 10^7$ (0.38), (*d*) $Ta = 6.0 \times 10^7$ (0.15) and (*e*) $Ta = 1.0 \times 10^8$ (0.12). Two-headed arrows indicate the theoretically predicted diameter of the columnar vortices L_{vortex} derived by Sakai (1997).

with v_{adv} indicating the horizontal advection speed of the columnar vortices. From these estimates the maximum value of v_{adv} is $O(0.1\text{–}1$ mm s$^{-1})$. With this, the time resolution for the vortex tracking of the horizontal cross-sections becomes $O(1$ s) under the present optical conditions.

In addition to the vertical average, the standard deviation of w, obtained from $\sigma(x, t)^2 = (1/H) \int_0^H [w(x, z, t) - \overline{w(x, t)}]^2 \, \mathrm{d}z$, gives another estimate of the vertical coherence. The standard deviations, $\sigma(x, t)$, for each of the periods in the images of figure 6 are presented in figure 7. At lower Ta settings, the high magnitude of $\sigma(x, t)$ indicates that w varies along the z axis. Accordingly, if the vertically straight (coherent) columns maintain their structures during this observation time, the magnitude of $\sigma(x, t)$ does not change at the same horizontal positions. For this reason, it is difficult to identify columns possessing system height structures for the lowest two Ta settings. A spatiotemporal integration (average) of $\sigma(x, t)$, $\overline{\sigma} = (1/LT) \int_0^L \int_0^T \sigma(x, t) \, \mathrm{d}x \, \mathrm{d}t$, suggests how stable the columnar vortices are, allowing the local characteristics of the duration of the columnar vortices to be quantified. This is because a smaller value of the spatiotemporal integration of the vertical variance signifies vertical coherence of the columnar vortices. The variations in $\overline{\sigma}$ with Ta are shown in figure 8; here, the dashed line shows the fitted curve calculated by the least-squares method. In the present study, the curve obtained is $\overline{\sigma}/U_f = 0.026 Ro^{0.47}$. As Ro approaches zero, the flow structures maintain vertical coherence here. For low Ro values there is a cellular regime (Cheng *et al.* 2015), where no visible vortex motion appears. This suggests that the results obtained in this analysis may be considered as reasonably accurate. In figure 8, the ratio of $\overline{\sigma}$ to U_f is $\sim$0.01 for the two highest Ta settings, with only 1 % of deviation from the free-fall velocity U_f.

To track the translational motion of the columnar vortices further, the points discussed in this section may be summarized as follows. The vortical structures exhibit two-dimensionality in the velocity distributions on the vertical cross-sections. Skewed structures along the z axis represent a three-dimensional turbulence-like state for the lowest Ta settings. With the time variation of w, a horizontal advection speed of the columns, v_{adv}, could be estimated. The estimated value of $O(0.1\text{–}1$ mm s$^{-1})$ suggests an appropriate time resolution for vortex tracking of every few seconds

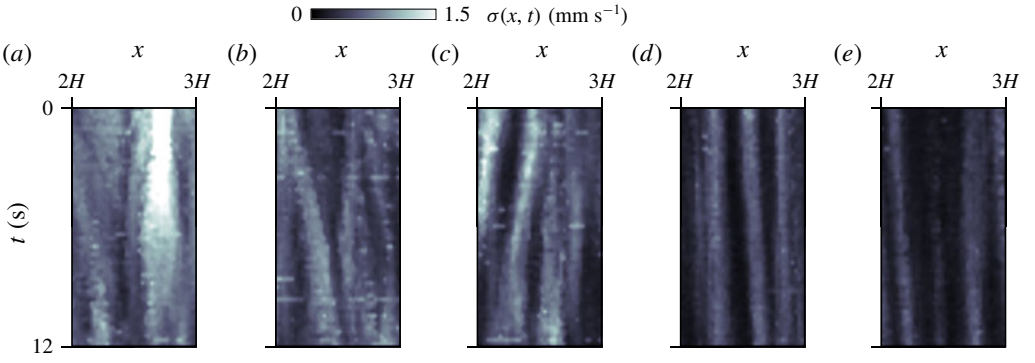

FIGURE 7. (Colour online) Time series of the standard deviations for the vertical velocity component at horizontal positions $2H < x < 3H$: (*a*) $Ta = 1.0 \times 10^6$ ($Ro = 1.20$), (*b*) $Ta = 6.0 \times 10^6$ (0.49), (*c*) $Ta = 1.0 \times 10^7$ (0.38), (*d*) $Ta = 6.0 \times 10^7$ (0.15) and (*e*) $Ta = 1.0 \times 10^8$ (0.12).

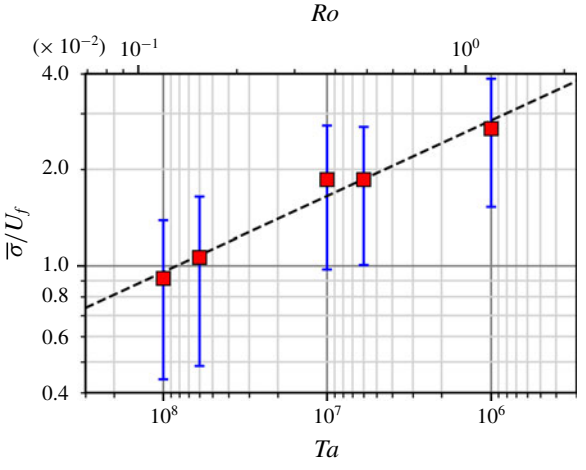

FIGURE 8. (Colour online) Variation of local duration characteristics $\overline{\sigma}$ plotted with error bars giving the standard deviation. Here, $\overline{\sigma}$ is normalized by the free-fall velocity U_f. The dashed line is a least-squares fit of $\overline{\sigma}/U_f = 0.026 Ro^{0.47}$.

ensuring that the detailed time resolution avoids erroneous tracking. In addition, the number of up-welling and down-welling vortices is also a good indicator of the flow state. An almost equal number of these in the same horizontal cross-section indicates (fully) developed CTC (see table 1). In summary, columnar vortices with $Ta \geqslant 1.0 \times 10^7$ ($Ro \leqslant 0.15$) ensure a horizontal translational motion of the columnar vortices in the present study.

4. Translational motion of columnar vortices

Next, we investigated the horizontal translational motion of the quasi-2-D columnar vortices. Unlike the PIV experiments (§ 3), circular fluid layers of different radii, $D =$ 80 and 190 mm, with the same height (thickness), $H = 40$ mm, were selected for examining the variation in the Froude number Fr for different values of the aspect

Pr	Ra	Γ	Ta	Ro	Fr
~ 7	1.0×10^7	2.00	1.0×10^7	0.38	4.0×10^{-3}
			3.0×10^7	0.22	1.2×10^{-2}
			1.0×10^8	0.12	4.0×10^{-2}
		4.75	1.0×10^7	0.38	9.5×10^{-3}
			3.0×10^7	0.22	2.9×10^{-2}
			1.0×10^8	0.12	9.5×10^{-2}

TABLE 2. Parameter settings for the vortex tracking experiments.

ratio Γ given the same rotational parameter settings. The experimental settings for the vortex tracking are listed in table 2. For set Ra value, $Ra = 1.0 \times 10^7$, three different Ta values in the range of $1.0 \times 10^7 \leqslant Ta \leqslant 1.0 \times 10^8$ were set. The corresponding values for Fr are in the range of $4.0 \times 10^{-3} \leqslant Fr \leqslant 9.5 \times 10^{-2}$. The effect of the centrifugal force has been empirically disregarded in cases of $Fr < 0.1$ (Cheng *et al.* 2018), and even the largest $Fr = 9.5 \times 10^{-2}$ in the present study is smaller than 0.1. This suggests that the effect of the centrifugal force may be considered negligible for all the conditions here according to empirical criteria.

4.1. *Vortex detection from horizontal temperature field*

Using encapsulated TLC particles, we were able to develop images of the temperature field (figure 9) to visualize the columnar vortices. Heated up-welling and cooled down-welling vortical structures are simply recognized as blue and red circular colour variations. For both Γ instances, finer and more organized structures with increasing Ta were found to be common changes. The horizontal scale of these vortical structures, denoted L_{vortex}, was predicted in previous work. At the onset of convection, Chandrasekhar (1961) using linear stability theory derived $L_{vortex} = cHTa^{-1/6}$ with the prefactor $c = 4.8$. Differently, Cheng *et al.* (2018) found $c = 2.4$ taking Ekman pumping into account with $Ta < 10^{14}$. In water experiments without a rigid top boundary, Boubnov & Golitsyn (1986) found an empirical scaling $L_{vortex} = Ra^{1/9}Ta^{-1/4}$ using the present notation. Sakai (1997) derived a theoretical scaling law by considering a physical model with two rigid boundaries and verified its adequacy experimentally. From his estimate, the horizontal scale of columnar vortices L_{vortex} is

$$L_{vortex} = 4.6H\frac{\delta_t^2}{2\delta_t^2 + 2\delta_t\delta_E + \delta_E^2}Ra^{1/3}Ta^{-3/8}, \tag{4.1}$$

where δ_t and δ_E denote the thickness of the thermal and Ekman boundary layers, respectively. Under set Ra conditions, L_{vortex} depends on only Ta. Our previous work (Noto *et al.* 2018) established a vortex determination method from instantaneous temperature fields using this estimate. On actual colour images, temperature values are reliably related to hue values, which directly shows the colour itself as a degree such as 0° for red, 120° for green and 240° for blue. This is useful for calibrating coloration to temperature, even though the uncertainty is not negligible. In the horizontal temperature fields obtained through this colour–temperature calibration, columnar vortices can be regarded as temperature undulations similar to a point spread function – a 2-D Gaussian distribution. This is because the temperature inside

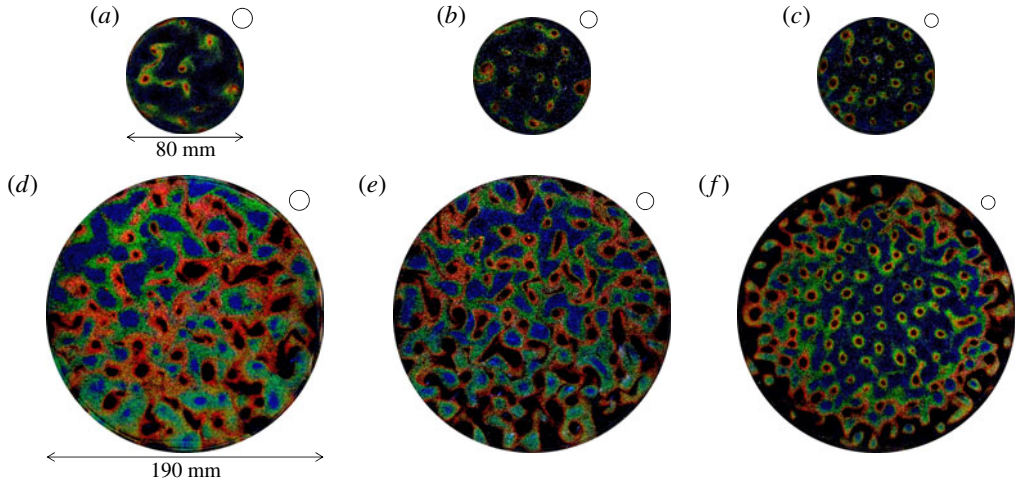

FIGURE 9. Examples of horizontal temperature fields visualized using encapsulated TLCs at $z=0.75H$ for (*a*) $Ta=1.0\times10^7$, (*b*) $Ta=3.0\times10^7$ and (*c*) $Ta=1.0\times10^8$ with $\Gamma=2.00$, and (*d*) $Ta=1.0\times10^7$, (*e*) $Ta=3.0\times10^7$ and (*f*) $Ta=1.0\times10^8$ with $\Gamma=4.75$. Open circles appearing on the upper right of each image indicate the horizontal scale of the columnar vortices predicted by Sakai (1997).

the down-welling (or up-welling) vortex gradually decreases (increases) towards the centre, and these facts result in the concave (convex) temperature distribution inside the vortex (e.g. figure 6 in Noto *et al.* 2018). Such concave or convex undulations can be extracted using pattern recognition techniques. In the present study, the same method was employed to detect columnar vortices of horizontal cross-sections.

4.2. *Statistical characteristics of advection velocity of columnar vortices*

As *Ro* approaches zero, the number of up-welling and down-welling vortices approaches a balance (Vorobieff & Ecke 2002). Assuming a balanced population and columnar vortices in vertical coherence, then only one, for example the down-welling, vortex motion needs to be investigated. (The centrifugal force discussed below, however, may affect statistical motions of up- and down-welling vortices and push vortices in the opposite directions.) Image acquisition was conducted for a one-hour period after reaching a fully developed flow state (more than 30 min from initiating the rotation). Around 1200 consecutive images and temperature fields were obtained. The nearest-neighbour method was employed to track the labelled vortices on the visualized temperature fields, in which two vortices having the shortest Euclidean distance between two consecutive images are linked. The vortex advection speed v_{adv} can then be obtained using

$$v_{adv}=\frac{|\boldsymbol{r}(t+\Delta t)-\boldsymbol{r}(t)|}{\Delta t}, \tag{4.2}$$

where $\boldsymbol{r}(t)$ denotes the vortex position vector obtained by the vortex detection method (Noto *et al.* 2018). The probability distributions of v_{adv} for all our settings of *Ta* and Γ were plotted and analysed (figure 10).

From all the conditions examined, the horizontal translational motion of columnar vortices is extremely slow compared with that of each of the flow fields (figure 10).

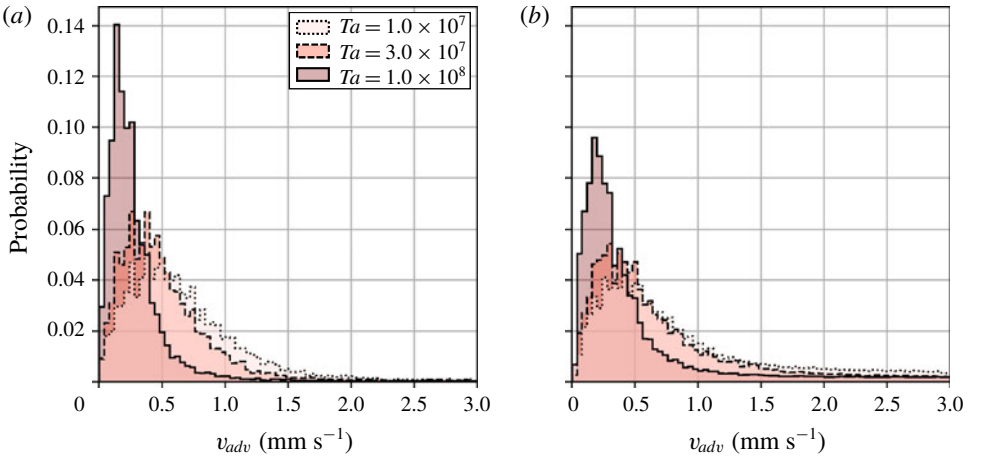

FIGURE 10. (Colour online) Probability distributions of horizontal advection speeds of columnar vortices v_{adv} for three different values of Ta; (*a*) $\Gamma = 2.00$ and (*b*) $\Gamma = 4.75$.

Specifically, v_{adv} is $O(10^{-1}$ mm s$^{-1})$ whereas a typical geostrophic velocity U_0 is $O(10^0$ mm s$^{-1})$. Moreover, v_{adv} decreases as Ta increases. This result is consistent with a transition from the CTC regime to the cellular regime as Ta increases. Basically, the distributions are quite similar for vessels of different aspect ratios, except for the highest Ta setting with the larger aspect ratio, where the corresponding Fr value is close to 0.1. Considering only the difference in the cylinder radii, an obvious difference under this condition may therefore come from the effect of the centrifugal force, even though all the present conditions are satisfying the conventional criterion to disregard any influence of centrifugal forces, $Fr < 0.1$. To confirm this possibility, the probability distribution for columnar vortices present inside the region $r \leqslant 40$ mm for the $\Gamma = 4.75$ vessel (corresponding to $\Gamma \leqslant 2.00$) is replotted (figure 11), here labelled $\Gamma = 4.75$ (inside) to separate the effect of centrifugal force. The distribution of $\Gamma = 4.75$ (inside) agrees well with that of $\Gamma = 2.00$. The probability distribution outside the region $r > 40$ mm, labelled $\Gamma = 4.75$ (outside), shifts slightly towards the higher-speed region compared with that for the inside region. In addition to this separately plotted histogram, the averaged radial components of advection speeds v_{adv} at each radial position, $\langle v_r(r)\rangle$, are examined to understand details of the effect of the centrifugal force. The averaged speed $\langle v_r(r)\rangle$ is defined as

$$\langle v_r(r)\rangle = \frac{1}{N}\sum_{i=1}^{N}(v_{xi}\cos\theta_i + v_{yi}\sin\theta_i), \tag{4.3}$$

plotted in figure 12, where v_x and v_y are the x and y components of the advection velocity of columnar vortices located at (r, θ) in polar coordinates. A gradual increase is observed in the larger vessel at $Ta = 1.0 \times 10^8$ (figure 12*b*) in concert with increases in r. Especially in the range of $0 \leqslant r < 60$ mm, $\langle v_r(r)\rangle$ is linearly proportional to the radial distance r with a slope of 0.0014 according to a least-squares fit in this range. It is noteworthy that the plot with the smaller vessel at $Ta = 1.0 \times 10^8$ fits the same line (slope) as shown in figure 12(*a*). Other conditions are everywhere in near $v_r = 0$ and it is difficult to identify any significant dependence on the radial position, except

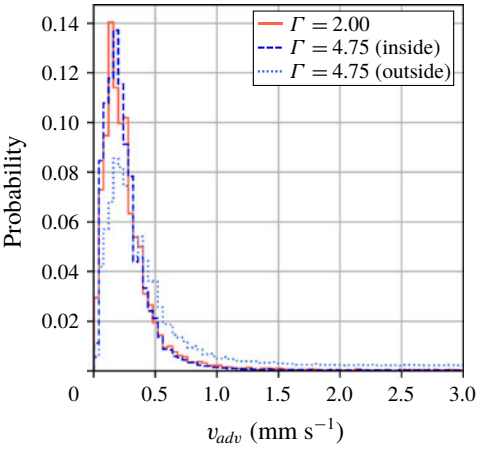

FIGURE 11. (Colour online) Probability distribution at $Ta = 1.0 \times 10^8$ with $\Gamma = 2.00$ (solid line) and separated plots of $\Gamma = 4.75$ from different regions: (inside) $r \leqslant 40$ mm (dashed line) and (outside) $r > 40$ mm (dotted line).

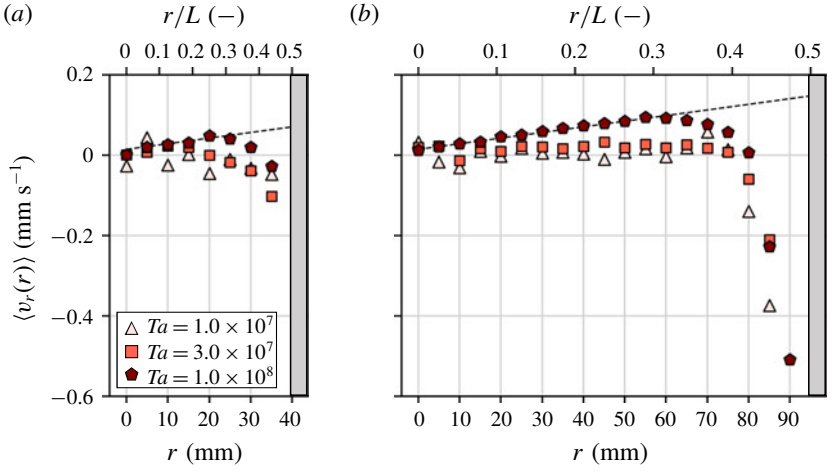

FIGURE 12. (Colour online) Radial position dependence of ensemble-averaged radial advection velocity $\langle v_r \rangle$: (*a*) $\Gamma = 2.00$ and (*b*) $\Gamma = 4.75$. Each plot is an average of 5 mm domains. Dashed line is $\langle v_r(r) \rangle = 0.0014r + 0.0143$ obtained by a least-squares fit.

for the vicinity of the wall. Sudden drops of the velocity in the region corresponding to radially inward movement start at $r \sim 0.35L$–$0.4L$ ($r \sim 28$–32 mm for $\Gamma = 2.00$ and $r \sim 67$–76 mm for $\Gamma = 4.75$) for all Ta conditions. These originate in repulsion by wall collisions. The standard deviations of each plot are roughly in the range of 0.2–0.6 mm s^{-1}, and increase as Ta decreases. These results suggest the conclusion that the centrifugal force working on each columnar vortex as a body force may be seen as the main reason for the differences in the distribution for this Ta setting, although heuristically the effects of the centrifugal force have been assumed negligibly small when $Fr < 0.1$ (Cheng *et al.* 2018). The influence of centrifugal forces on the vortex motion will be discussed in the next section.

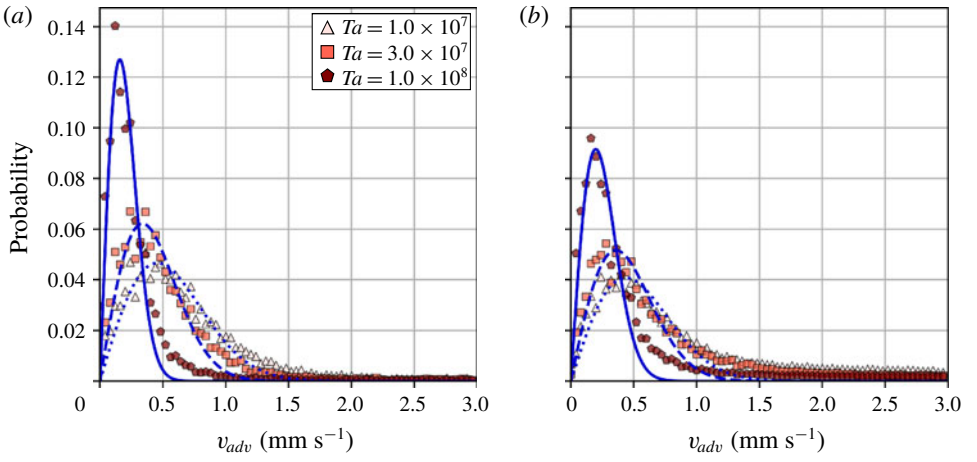

FIGURE 13. (Colour online) Probability density functions fitted by the Maxwell distribution; the original probability density function data are from figure 10 for the three different Ta settings with (*a*) $\Gamma = 2.00$ and (*b*) $\Gamma = 4.75$ vessels.

An approximate evaluation of the probability density distributions suggests that their shape is similar to a Maxwell distribution assuming a probability density function with more frequent low energies (speed) and fewer high energies. If this is reasonably satisfied, translational motion of the columnar vortices can be regarded as diffusive motion, similar to Brownian motion. An attempt to fit the histograms (figure 10) by the Maxwell distribution,

$$P_M(v) = Av \exp(-v^2/B), \tag{4.4}$$

was performed using the least-squares approximation (figure 13). The classical assumptions underpinning this distribution for the particle speed are that the particles initially move randomly, and form an idealized gas that is spatially homogeneous (independent of their position) and which is isotropic. Quite large deviations from the fitted curves are seen, especially in the high-speed region. Table 3 lists the fitting constants, A and B, and three speeds of vortex advection, here denoted v_{mp}, v_{ave} and v_{rms}. They signify respectively the most probable speed satisfying $\mathrm{d}P(v_{mp})/\mathrm{d}v = 0$, the average speed and the root-mean-squared speed. For brevity, v_{adv} is expressed as v in the above equation. These velocities may also be calculated from the fitted curves; v_{mp} is given as $v_{mp} = \sqrt{B}$. It is clear that the speeds depend on Ta conditions, although the quality of the fit by the Maxwell distribution with classical assumptions is not perfect. The reasons for the discrepancy will be assessed in the next section and form the main purpose of this paper.

4.3. *Tracking of the multi-time-scale behaviour of columnar vortices*

With only the instantaneous observations of the motion of columnar vortices, the deviations from the probability distributions in the Maxwell distributions are difficult to explain. To provide a more detailed description of the vortex motion, a quantification of the differences between actual and idealized particles was performed. The differences arise because of the presence of strong mutual interactions and

Γ	Ta	A (s mm^{-1})	B (mm^2 s^{-2})	v_{mp} (mm s^{-1})	v_{ave} (mm s^{-1})	v_{rms} (mm s^{-1})
2.00	1.0×10^7	0.168	0.416	0.645	0.671	0.818
	3.0×10^7	0.303	0.229	0.478	0.532	0.675
	1.0×10^8	1.326	0.0499	0.223	0.293	0.427
4.75	1.0×10^7	0.154	0.381	0.617	0.884	1.138
	3.0×10^7	0.237	0.257	0.507	0.718	0.947
	1.0×10^8	0.760	0.0789	0.281	0.501	0.764

TABLE 3. Advection speeds of columnar vortices.

external (centrifugal) forces. Rather than the analysis of discrete sequences of observations, continuous observations of the vortex motion would serve this purpose. In preparation for this, the lifetime t_{life} of columnar vortices needs to be determined to establish the time scales in which the mutual interactions are appreciable. For the time intervals where an individual vortex is tracked, t_{life} may also be established (see Noto *et al.* 2018); in the determination a vortex is deemed to be created at its first detection in a temperature field, and its disappearance through merging defines the end of its presence in the series of observations. The probability distribution for t_{life} during one hour of observations is then extracted based on this definition (figure 14). Columnar vortices have lifetimes distributed mainly from 10 to 100 s in both vessels here. For $\Gamma = 2.00$ in figure 14(*a*), there is a clear Ta dependence on t_{life}; vortices have shorter lifetimes at lower Ta values. With $\Gamma = 4.75$ in figure 14(*b*), however, the Ta dependence is less clear. The reason may be because centrifugal forces are affecting the vortex motion. The sampled number of vortices for the smaller vessel is smaller than that for the larger vessel; however, the two plots show similar advection changes, suggesting that the advection may be determined by the advection speed in the finite fluid layer and interactions with the surrounding vortices. The differences along the vertical axis are suggested to stem from the sampled number of vortices and to arise from the differences in the aspect ratio. In the present conditions, frequent merging events have been reported in several previous experimental works (Boubnov & Golitsyn 1986; Zhong *et al.* 1993; Noto *et al.* 2018) and numerical works (Julien *et al.* 1996; Pieri *et al.* 2016) as arising from the absence of sheath structures with vorticities of opposite signs. The historicity, position dependence and strong mutual interaction within the surroundings may be the cause of the discrepancies appearing in the quality of the fit described in the previous section. Considering the variations in vortex motion which depend on the observation time scale, vortex lifetimes are very important. This is because the forces affecting the vortices and the heat carried by the vortices are both dependent on the vortex lifetime. From the observed phenomena and the various lifetimes of the vortices, three time scales may be postulated: a short time scale $O(10^0$–10^1 s) where no vortex–vortex interactions occur, an intermediate time scale $O(10^1$–10^2 s) where strong mutual interactions occur and a long time scale $O(10^2$–10^3 s) where the effects of external forces (centrifugal forces) emerge.

To further substantiate this, an analysis of the instantaneous vortex behaviour, as well as vortex tracking by time scales $O(> 10^1$ s) in which the various forces act on the vortex motion, including their advection history, must be conducted. Noto *et al.* (2018) reported quasi-regular vortex arrangements obtained in 90 s periods for larger Ta settings, and suggested the possibility of describing vortex motion as an n-body problem. Path lines of vortex advection at these time scales (during $30\Delta t$; 90 s) were

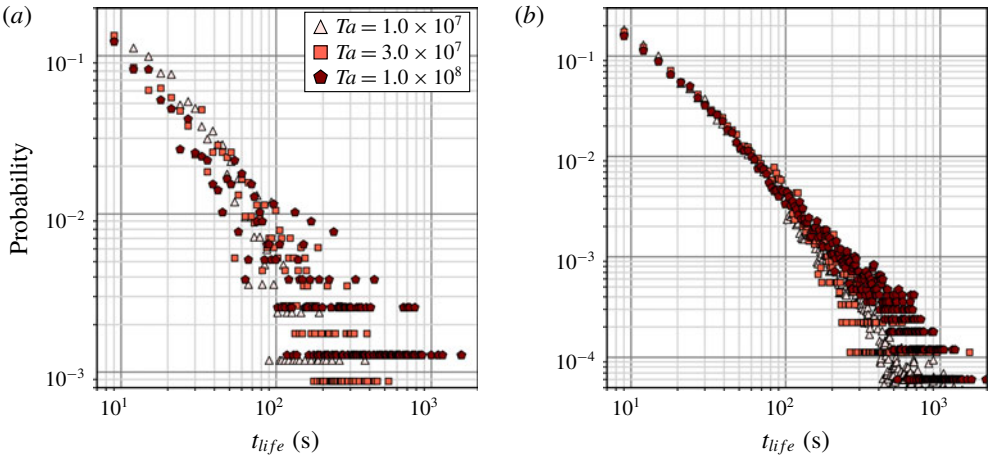

FIGURE 14. (Colour online) Probability distributions of lifetimes t_{life} of columnar vortices for (*a*) $\Gamma = 2.00$ and (*b*) $\Gamma = 4.75$.

plotted (figure 15). In figure 15, path lines of down-welling columns present in one period (90 s) were cropped and redrawn using colour coding to represent the elapsed time. Depending on the number of vortices, the number of path lines increases with *Ta*, and from figure 10 the displacement in one time step (3 s) becomes larger as *Ta* decreases. The path lines in figure 15(*a*,*b*,*d*,*e*) appear to be random walks, with no directivity. With high *Ta* values in both vessels here (figure 15*c*,*f*), the path lines show weak regularity with the directions of movement restricted by surrounding path lines. As two vortices of opposing vorticity cannot merge (Sprague *et al.* 2006), this suggests why so few path lines are observed. With the presence of adjacent up-welling vortices, the motion of down-welling vortices tracked here is directional. Further, the repulsion from up-welling vortices cannot be ignored in this situation, as Julien *et al.* (1996) observed when strong vortex–vortex interactions were present. The path lines for high *Ta* values may, therefore, be assumed not to represent random motion as shown by Brownian particles.

In addition to the analysis at the intermediate time scales $O(10^1$–10^2 s), vortex tracking over much longer time scales $O(10^2$–10^3 s) may be performed simply by using the vortex detection method from the images (Noto *et al.* 2018). With the larger vessel ($\Gamma = 4.75$) generating centrifugal force effects ($Fr \sim 0.1$) from rapid rotations, such effects appear in the path lines for long times of presence $O(10^2$ s) (figure 16), and in figure 16, for clarity, only trajectories longer than 450 s are plotted. In figure 16(*a*), the vortex trajectories appear with repeated jerky movements, in the shape of random walks, and in figure 16(*b*) there are numerous trajectories that are largely directed radially outward. This radial motion is not straight, but features a zigzag pattern as the columns are strongly affected by their other surrounding vortices, as discussed earlier for figure 15. Columnar vortices in the large-aspect-ratio vessel behave as Brownian particles over short time scales $O(10^0$–10^1 s), and are affected by centrifugal forces over longer time scales $O(10^2$–10^3 s). As figure 11 also clearly shows, the influence of centrifugal forces on vortex motion appears only over the long time scales. To explain the details of this random-walk-like motion, a further discussion of its statistical nature will be given in the next section.

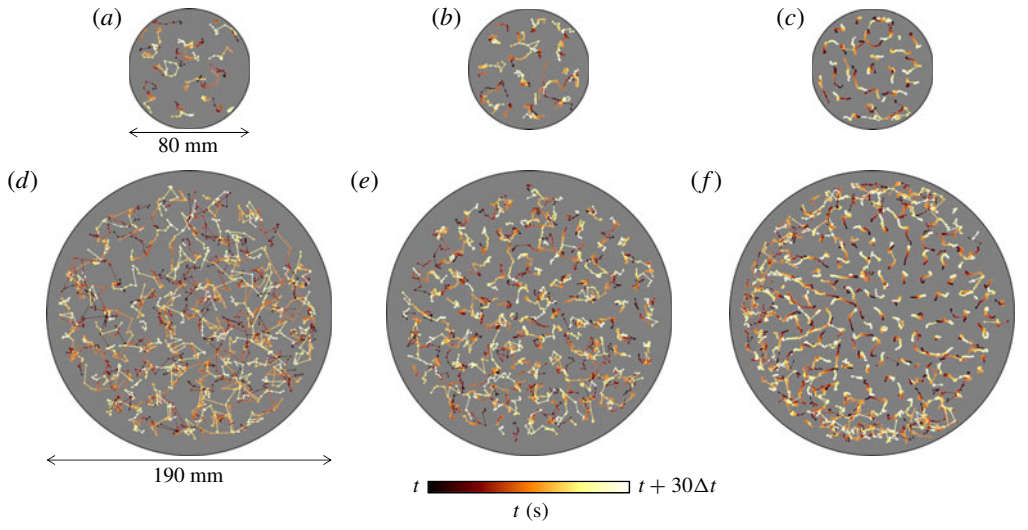

FIGURE 15. (Colour online) Path lines for advections of the columnar vortices for 90 s: (*a*) $Ta = 1.0 \times 10^7$, (*b*) $Ta = 3.0 \times 10^7$ and (*c*) $Ta = 1.0 \times 10^8$ with $\Gamma = 2.00$, and (*d*) $Ta = 1.0 \times 10^7$, (*e*) $Ta = 3.0 \times 10^7$ and (*f*) $Ta = 1.0 \times 10^8$ with $\Gamma = 4.75$, where the evolution of the path lines is displayed using colour coding. Backgrounds are grey for better visibility.

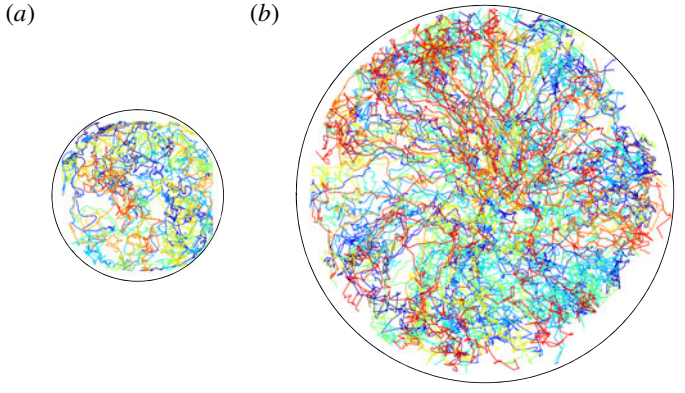

FIGURE 16. Examples of path lines of columnar vortices persisting over 450 s with $Ta = 1.0 \times 10^8$ for (*a*) $\Gamma = 2.00$ and (*b*) $\Gamma = 4.75$. Path lines are individually colour coded.

5. Statistical analysis of the translational motion

5.1. *Horizontal diffusive motion of columnar vortices*

Although the probability distributions of vortex advection speeds do not fit a purely Maxwell distribution with its classical assumptions, a random-walk-like motion, however, is observed in the path lines in figures 15 and 16. Based on this, there is the possibility that it will be possible to describe the vortex motion as diffusive motion. Brownian motion (random walk) shown by molecules in a thermal equilibrium state is one example of commonly occurring normal diffusive motion, natural diffusion without acceleration or deceleration. In other situations of turbulent diffusive arrangements, random Lagrangian particle motion can be represented as diffusive

motion arising from macroscopic fluctuations (Solomon, Weeks & Swinney 1993). Diffusive motion is characterized by determining the mean-squared displacement (MSD):

$$\mathrm{MSD} = \langle \delta \boldsymbol{r}(t)^2 \rangle = \frac{1}{N} \sum_{i=1}^{N} [\boldsymbol{r}_i(t) - \boldsymbol{r}_i(0)]^2, \tag{5.1}$$

where $\delta \boldsymbol{r}(t)$ is the displacement from the initial vortex position $\boldsymbol{r}(0)$ with time t and angular brackets $\langle\ \rangle$ indicate an ensemble average. The time dependence of the MSD for normal diffusion processes is given by

$$\langle \delta \boldsymbol{r}(t)^2 \rangle \sim t^{\gamma} \quad \text{with } \gamma = 1. \tag{5.2}$$

Instances of $\gamma \neq 1$ indicate anomalous diffusion: super-diffusion ($1 < \gamma < 2$) influenced by acceleration and sub-diffusion ($0 < \gamma < 1$) influenced by deceleration. Diffusive motion commonly indicates the motion of very small molecules (particles). Meuel *et al.* (2012) performed an MSD analysis to investigate the motion of tropical cyclones, and quantification of diffusive motions of such macroscopic structures is also informative to understand the power sources and time scales dominating the motion. In the present study, an MSD analysis was applied to the horizontal motion of the columnar vortices to be able to discuss the complicated motion presently accepted as diffusive motion; the calculated MSDs are plotted in figure 17. To ensure the reliability of the statistics, only ensemble averages with more than 100 vortices are plotted in figure 17. This results in some discrepancy with the lifetimes shown in figure 14. The common feature to note in figure 17 is the relatively large MSD values appearing at low *Ta* settings for both vessels with their different aspect ratios. The magnitude of the MSD reflects the speed of the diffusive motion of the columnar vortices, the speed of movements of the columns moving away from a specific position, the coefficient of diffusion $D(t)$, which can be obtained from

$$D(t) \equiv \frac{\langle \delta \boldsymbol{r}(t)^2 \rangle}{2\Delta t}. \tag{5.3}$$

Here, Δt is the time interval of the vortex tracking; in the present case, $\Delta t = 3$ s. For both vessels, lower *Ta* settings show larger $D(t)$ at $O(10^0$–10^2 s). The calculated $D(t)$ are in the range of 10^{-7}–10^{-6} m^2 s^{-1}, with the coefficient of viscous diffusion $\nu = 1.0 \times 10^{-6}$ m^2 s^{-1}, and the coefficient of thermal diffusion $\kappa = 1.4 \times 10^{-7}$ m^2 s^{-1}. For the vessel with $\Gamma = 2.00$, $D(t)$ decreases as *Ta* increases over the observed period. In addition to this *Ta* dependence of the coefficient of diffusion, time variations in the slopes, $\gamma > 1$ in $O(10^0$–10^1 s), $\gamma < 1$ in $O(10^1$ s) and $\gamma \geqslant 1$ in $O(10^1$–10^2 s), are also observed in the smaller vessel. However, for $\Gamma = 4.75$, there is no clear *Ta* dependence, especially over long time scales. There are clear differences at the highest *Ta* values in the larger vessel (filled pentagons in figure 17*b*); the high *Ta* MSD plots cross the two other lower *Ta* conditions because of an abrupt increase in γ around $O(10^2$ s), from $\gamma \sim 1$ in $O(10^1$ s) to $\gamma \sim 1.6$ in over $O(10^2$ s). This difference appears only for the highest *Ta* and may be ascribed to the effect of centrifugal forces. Centrifugal force accelerates the vortex motion in the radial direction, making the columnar vortices more easily diffuse and this results in the super-diffusive motion. Further, the intermediate time scale $O(10^1$ s) shows slight, but gradual decreases in γ for all settings. Viewing path lines drawn at the intermediate time scale (for 90 s) in figure 15, there is some regularity in the path lines, a result of the mutual interactions between adjacent vortices. This behaviour corresponds to a deceleration of the horizontal motion of the columnar vortices appearing as sub-diffusive motion, $\gamma < 1$. Further discussion of this is provided below.

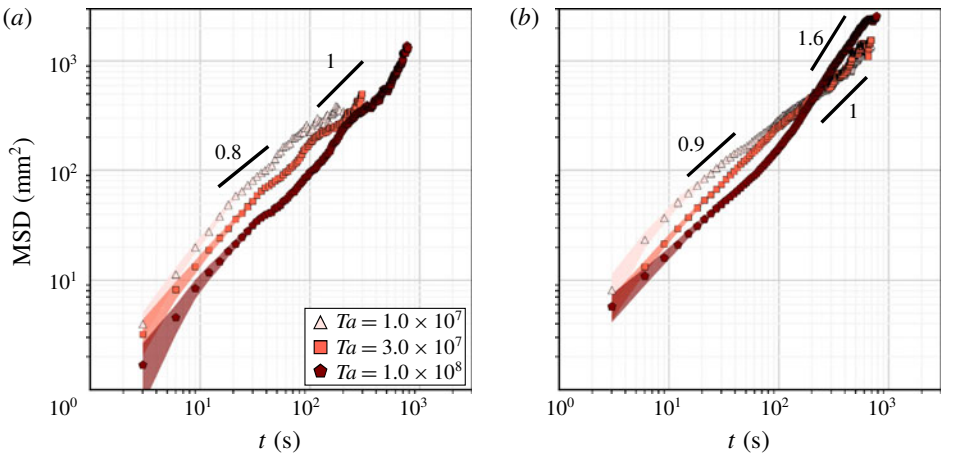

FIGURE 17. (Colour online) The MSD $\langle \delta \boldsymbol{r}(t)^2 \rangle$ of the horizontal motion of columnar vortices for different Ta values with (*a*) $\Gamma = 2.00$ and (*b*) $\Gamma = 4.75$. The numbers accompanying the black solid lines are the γ values. Faded-colour areas behind each plot indicate the standard deviation of the MSD.

5.2. *Anomalous diffusion of columnar vortices*

For the higher Ta settings, a smooth MSD plot (figure 17) is obtained over time scales of $O(> 10^2$ s) as the number of long-lived vortices is large. It is however impossible to obtain smooth curves for the lower Ta settings because the lifetimes of the columnar vortices are relatively short making it difficult to record a sufficiently large number of data points for ensemble averaging. With the slope of the MSD for $\gamma \neq 1$, the translational motion of the columnar vortices cannot be considered a pure normal diffusive motion like the random walk displayed by Brownian particles. In particular, as discussed at the end of § 5.1, intermediate time scales $O(10^1$ s) for $\Gamma = 2.00$ and $Ta = 1.0 \times 10^8$ show slight decreases in γ to $\gamma \sim 0.8$–0.9. For this setting, the vortex motion represented as the path lines in figure 15 is restricted by the adjacent vortices of opposite vorticities. The two types of down-welling and up-welling vortices do not merge, but assume a checkerboard (regular grid) pattern in the vortex arrangement. The random-walk-like motion of a down-welling vortex follows the patterns suggested by the arrow in figure 18(*a*). This may be interpreted to show that the vortex motion is enclosed by a barrier of different-type vortices at this intermediate time scale (figure 18*b*).

To understand this anomaly in the diffusive vortex motion, the characteristics of columnar vortices different from Lagrangian particles must be considered because the columns are macroscopic flow structures, and are continuous phase to the ambient fluid. For instance, the size of the columnar vortices must be considered unlike negligibly small particles. In addition, columnar vortices have a wide range of lifetimes (observable lives). Depending on the time of observation (lifetime), the observed diffusive motion may vary as strong mutual interactions shown as regularities in figure 15. It may be that the relevant mutual interactions from the surroundings appear at the collision of one vortex with another, making it necessary to consider the mean free time τ of the columnar vortices. In this case, τ is the length of time between the collisions of one vortex and another and is given by $\tau = l/v_{mp}$, with l the mean free distance. Assuming that columnar vortices fill the entire fluid layer,

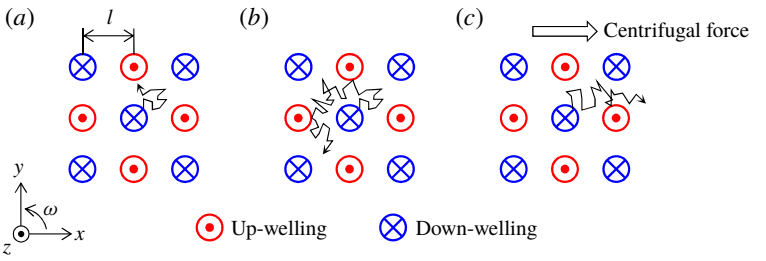

FIGURE 18. (Colour online) Conceptual diagram of the vortex motion without centrifugal force effects for (*a*) $t_{life} < \tau$ and (*b*) $t_{life} \geqslant \tau$, and with centrifugal force effects for (*c*) $t_{life} \gg \tau$.

Γ	Ta	v_{mp} (mm s^{-1})	L_{vortex} (mm)	τ (s)
2.00	1.0×10^7	0.645	16.5	25.6
	3.0×10^7	0.478	11.7	24.5
	1.0×10^8	0.223	9.34	41.9
4.75	1.0×10^7	0.617	16.5	26.7
	3.0×10^7	0.507	11.7	23.1
	1.0×10^8	0.281	9.34	33.2

TABLE 4. Mean free time for columnar vortices for different Γ and Ta values.

l is equivalent to L_{vortex}, and based on this the calculated τ durations are listed in table 4.

For $t_{life} > \tau$, the vortex motion is affected by different adjacent vortices, as they repulse each other. As a result, the repulsions would yield an enclosure effect which slows the vortex motion and prevents unimpeded normal diffusive motion (figure 18*b*). The mean free times τ listed in table 4 indicate that such an effect appears at $O(10^1$ s). From figure 17, the sub-diffusive trend, $\gamma \sim 0.8$–0.9, clearly reflects this effect, and the columnar vortices diffuse little over intermediate time scales.

Under conditions without the effect of centrifugal forces (or even negligibly small effects), there is no very large difference in τ between the two vessels with different aspect ratios here. When centrifugal forces are working (at $Ta = 1.0 \times 10^8$ for $\Gamma = 4.75$), τ becomes shorter than that of $\Gamma = 2.00$ because the horizontal motion is accelerated by this externally imposed force. The centrifugal forces move the down-welling vortices outward in the radial direction because the density of cold down-welling vortices is larger (figure 18*c*). The up-welling vortices (lighter than the down-welling ones) are moved radially inwards in the vessel. Frequent collisions, which oppose free advection of columns towards each other, due to these radial accelerations are the reasons why τ is shorter for the larger vessel than for the smaller vessel. In addition, for the larger vessel, the columnar vortex in the system undergoes super-diffusive motion due to the centrifugal forces over the long time scales $O(> 10^2$ s). A large value of γ, $\gamma \sim 1.6$, as indicated in figure 17, supports this conclusion even though the mean free time τ is shorter when a centrifugal force is working than when it is absent. The large value of γ for longer time scales $O(> 10^2$ s) observed in figure 17(*b*) with the highest Ta value would be sustained or further enhanced for vessels of larger horizontal extent, and yield super-diffusive motion as in Lévy flights

(e.g. Shlesinger, Zaslavsky & Klafter 1993; Solomon *et al.* 1993), a repetition of stop–go motion. The value of γ asymptotes towards 2 indicating a ballistic diffusion if the experiment could be conducted in a vessel of infinite horizontal extent.

Columnar vortices are not completely isolated from their surroundings but are part of a continuous structure in the surrounding fluid as they are macroscopic flow structures as described above. Therefore, it is impossible to consider these as perfect rigid-body columns of tiny floating particles as discussed above. The unclearly delineated borders and variable body, which are easily affected by the surroundings, are the reasons why clear flight events are not observed. Merging events of the same type of vortices are also thought to be a reason. Commonly, a vortex is surrounded by two types of vortices with a somewhat loose regularity (figure 18). Vortices with opposite vertical flow directions repel each other, whereas the same types of vortices merge (e.g. Zhong *et al.* 1993; Julien *et al.* 1996; Pieri *et al.* 2016; Noto *et al.* 2018). Ideally, the probability that a vortex collides with either type of vortex is almost even for high *Ta* values, because the populations of up-welling and down-welling vortices are almost the same (Vorobieff & Ecke 2002; Sprague *et al.* 2006). Opposite-type vortices behave as a barrier preventing normal (random) diffusive motion. The geometric (quasi-polygonal) path lines (figure 15*c*,*f*) are formed by this directivity because of the enclosure effect. Further, merging events do not affect the vortex motion and do not appear in the MSD analysis (figure 17), but only affect the lifetimes (figure 14). These various characteristics of the columnar vortices enable some balance resulting in the γ exponent close to unity.

6. Concluding remarks

To characterize horizontal translational motion of columnar vortices formed in rotating RBC, laboratory experiments using water confined in two vessels of different radii were conducted. With different aspect ratios, the influence of the centrifugal forces was investigated while keeping other non-dimensional parameter values fixed. Direct velocity field measurements in vertical cross-sections by PIV were made to identify practical rotational parameter values suggesting the formation of prominent columnar vortices by evaluating localized characteristics of the columnar vortices. In the present experimental configuration, columnar vortices formed when the convective Rossby number $Ro < 0.4$ ensured vertical coherence of the velocity field. For these settings, experiments tracking the columnar vortices in horizontal cross-sections were conducted using TLC visualization. The horizontal motion was tracked for periods up to 10^3 s. The instantaneous profiles of the horizontal advection speeds were difficult to characterize as random-walk-like motion as represented in Maxwell distributions. In observing the temporal motion of the columns, intense mutual interactions such as merging and repulsion among the vortices appeared as some regularity of vortex path lines were observed. Further, the effect of centrifugal forces appeared on time scales of $O(10^2$ s) even though all the present conditions should in practice be negligible contributions of the centrifugal force ($Fr < 0.1$). The MSD analyses of the horizontal motions of the columnar vortices showed that the motions may be described as anomalous diffusive motion. Presenting a combination of the lifetime of columnar vortices and various other characteristics such as generation, disappearance, merging and repulsion, the horizontal motions of the columnar vortices were categorized as different diffusive motions: sub-diffusive motion (decelerated advection) due to an enclosure effect arising from the surroundings at $O(10^1$–10^2 s) and super-diffusive motion (radially accelerated advection) because of centrifugal forces at $O(> 10^2$ s).

Acknowledgements

The authors acknowledge Dr Y. Sato and Professor K. Julien for fruitful discussions and helpful advice.

REFERENCES

ABDULLAH, N., TALIB, A. R. A., JAAFAR, A. A., SALLEH, M. A. M. & CHONGA, W. T. 2010 The basics and issues of thermochromic liquid crystal calibrations. *Exp. Therm. Fluid Sci.* **34**, 1089–1121.

AURNOU, J. M., CALKINS, M. A., CHENG, J. S., JULIEN, K., KING, E. M., NIEVES, D., SODERLUND, K. M. & STELLMACH, S. 2015 Rotating convective turbulence in earth and planetary cores. *Phys. Earth Planet. Inter.* **246**, 52–71.

BOUBNOV, B. M. & GOLITSYN, G. S. 1986 Experimental study of convective structures in rotating fluids. *J. Fluid Mech.* **167**, 503–531.

CHANDRASEKHAR, S. 1961 *Hydrodynamic and Hydromagnetic Stability*. Oxford University Press.

CHENG, J. S., AURNOU, J. M., JULIEN, K. & KUNNEN, R. P. J. 2018 A heuristic framework for next-generation models of geostrophic convective turbulence. *Geophys. Astrophys. Fluid Dyn.* **112** (4), 277–300.

CHENG, J. S., STELLMACH, S., RIBEIRO, A., GRANNAN, A., KING, E. M. & AURNOU, J. M. 2015 Laboratory-numerical models of rapidly rotating convection in planetary cores. *Geophys. J. Intl* **201**, 1–17.

GRANNAN, A. M., FAVIER, B., LE BARS, M. & AURNOU, J. M. 2016 Tidally forced turbulence in planetary interiors. *Geophys. J. Intl* **208** (3), 1690–1703.

GROOMS, I., JULIEN, K., WEISS, J. B. & KNOBLOCH, E. 2010 Model of convective Taylor column in rotating Rayleigh–Bénard convection. *Phys. Rev. Lett.* **104**, 224501.

HORN, S. & AURNOU, J. M. 2018 Regimes of Coriolis–centrifugal convection. *Phys. Rev. Lett.* **120** (20), 204502.

JONES, C. A. 2011 Planetary magnetic fields and fluid dynamos. *Annu. Rev. Fluid Mech.* **43**, 583–614.

JULIEN, K., AURNOU, J. M., CALKINS, M. A., KNOBLOCH, E., MARTI, P., STELLMACH, S. & VASIL, G. M. 2016 A nonlinear model for rotationally constrained convection with Ekman pumping. *J. Fluid Mech.* **798**, 50–87.

JULIEN, K., LEGG, S., MCWILLIAMS, J. & WERNE, J. 1996 Rapidly rotating turbulent Rayleigh–Bénard convection. *J. Fluid Mech.* **322**, 243–273.

JULIEN, K., RUBIO, A. M., GROOMS, I. & KNOBLOCH, E. 2012 Statistical and physical balances in low Rossby number Rayleigh–Bénard convection. *Geophys. Astrophys. Fluid Dyn.* **106**, 392–428.

KUNNEN, R. P. J., CLERCX, H. J. H. & GEURTS, B. J. 2010 Vortex statics in turbulent rotating convection. *Phys. Rev.* E **82** (3), 036306.

KUNNEN, R. P. J., CORRE, Y. & CLERCX, H. J. H. 2014 Vortex plume distribution in confined turbulent rotating convection. *Eur. Phys. Lett.* **104** (5), 54002.

LIU, Y. & ECKE, R. E. 2009 Heat transport measurements in turbulent rotating Rayleigh–Bénard convection. *Phys. Rev.* E **80**, 036314.

MEUEL, T., PRADO, G., SEYCHELLES, F., BESSAFI, M. & KELLAY, H. 2012 Hurricane track forecast cones from fluctuations. *Sci. Rep.* **2**, 446.

NOTO, D., TASAKA, Y., YANAGISAWA, T., PARK, H. J. & MURAI, Y. 2018 Vortex tracking on visualized temperature fields in a rotating Rayleigh–Bénard convection. *J. Vis.* **21**, 987–998.

PIERI, A. B., FALASCA, F., HARDENBERG, J. V. & PROVENZALE, A. 2016 Plume dynamics in rotating Rayleigh–Bénard convection. *Phys. Lett.* A **380**, 1363–1367.

RAJAEI, H., KUNNEN, R. P. J. & CLERCX, H. J. H. 2017 Exploring the geostrophic regime of rapidly rotating convection with experiments. *Phys. Fluids* **29** (4), 045105.

RAO, Y. & ZANG, S. 2010 Calibrations and the measurement uncertainty of wide-band liquid crystal thermography. *Meas. Sci. Technol.* **21**, 015105.

SAKAI, S. 1997 The horizontal scale of rotating convection in the geostrophic regime. *J. Fluid Mech.* **333**, 85–95.

SHLESINGER, M. F., ZASLAVSKY, G. M. & KLAFTER, J. 1993 Strange kinetics. *Nature* **363** (6424), 31–37.

SOLOMON, T. H., WEEKS, E. R. & SWINNEY, H. L. 1993 Observation of anomalous diffusion and Lévy flights in a two-dimensional rotating flow. *Phys. Rev. Lett.* **71** (24), 3975–3978.

SPRAGUE, M., JULIEN, K., KNOBLOCH, E. & WERNE, J. 2006 Numerical simulation of an asymptotically reduced system for rotationally constrained convection. *J. Fluid Mech.* **551**, 141–174.

STELLMACH, S., LISCHPER, M., JULIEN, K., VASIL, G., CHENG, J. S., RIBEIRO, A., KING, E. M. & AURNOU, J. M. 2014 Approaching the asymptotic regime of rapidly rotating convection: boundary layers versus interior dynamics. *Phys. Rev. Lett.* **113**, 254501.

STEVENS, R. J. A. M., CLERCX, H. J. H. & LOHSE, D. 2012 Breakdown of the large-scale wind in $\gamma = 1/2$ rotating Rayleigh–Bénard flow. *Phys. Rev.* E **86**, 056311.

STEVENS, R. J. A. M., CLERCX, H. J. H. & LOHSE, D. 2013 Heat transport and flow structure in rotating Rayleigh–Bénard convection. *Eur. J. Mech. (*B*/Fluids)* **40**, 41–49.

VOROBIEFF, P. & ECKE, R. E. 1998 Vortex structure in rotating Rayleigh–Bénard convection. *Physica* D **123**, 153–160.

VOROBIEFF, P. & ECKE, R. E. 2002 Turbulent rotating convection: an experimental study. *J. Fluid Mech.* **458**, 191–218.

WEISS, S. & AHLERS, G. 2011 Heat transport by turbulent rotating Rayleigh–Bénard convection and its dependence on the aspect ratio. *J. Fluid Mech.* **309**, 1–20.

WIBERG, R. & LIOR, N. 2004 Errors in thermochromic liquid crystal thermometry. *Rev. Sci. Instrum.* **75**, 2985–2994.

ZHONG, F., ECKE, R. E. & STEINBERG, V. 1993 Rotating Rayleigh–Bénard convection: asymmetric modes and vortex states. *J. Fluid Mech.* **249**, 135–159.